COMPARATIVE MODAL ANALYSIS OF SIEVE HARDWARE DESIGNS

by

Nathaniel Thompson

MSOL 299

A project report submitted to the

Henry Samueli School of Engineering and Applied Science

in partial fulfillment of the requirements for the degree of

Master of Science in Mechanics of Structures

UNIVERSITY OF CALIFORNIA LOS ANGELES

SCHOOL OF ENGINEERING AND APPLIED SCIENCE

June, 2012

The project report “Comparative Modal Analysis of Sieve Hardware Designs” presented by Nathaniel Thompson is approved.

_____

Dr. Jiun-Shyan Chen

Date: _____

Acknowledgments

I would like to express my sincere gratitude to the many people involved in this project.

First, I would like to acknowledge the advice of Dr. Jiun-Shyan Chen, whose guidance helped to formulate and focus my analysis, and then to interpret and expand on my results.

I would also like to thank my co-workers, Cambria Logan of JPL, and Daniel Sunshine formerly of JPL, for helping me to understand the background and requirements of the CHIMRA system.

Finally, I would thank all of my friends and family. It was their everlasting patience, understanding, and support throughout this project and over the course of my degree that made this endeavor possible.

This research was carried out at the Jet Propulsion Laboratory, California Institute of Technology, under a contract with the National Aeronautics and Space Administration.

Table of Contents

Abstract

The CMTB Thwacker hardware operates as a testbed analogue for the Flight Thwacker and Sieve components of CHIMRA, a device on the Curiosity Rover. The sieve separates particles with a diameter smaller than 150 microns for delivery to onboard science instruments. The sieving behavior of the testbed hardware should be similar to the Flight hardware for the results to be meaningful. The elastodynamic behavior of both sieves was studied analytically using the Rayleigh Ritz method in conjunction with classical plate theory. Finite element models were used to determine the mode shapes of both designs, and comparisons between the natural frequencies and mode shapes were made. The analysis predicts that the performance of the CMTB Thwacker will closely resemble the performance of the Flight Thwacker within the expected steady state operating regime. Excitations of the testbed hardware that will mimic the flight hardware were recommended, as were those that will improve the efficiency of the sieving process.

List of Figures

List of Tables

1.0 Notations

1.1 Acronyms

CHIMRA	Collection and Handling for In situ Martian Rock Analysis
CMTB	Challenge Materials Testbed
JPL	Jet Propulsion Laboratory
MSL	Mars Science Laboratory
QMDT	Qualification Model Dirty Test
SA/SPAH	Sample Acquisition, Processing and Handling

1.2 Definition of Symbols

The following nomenclature is used in this paper. Any consistent set of units can be used for the physical quantities. For reference purposes, the units are given in the SI unit system.

w	=	Lateral deflection of plate, mm
x,y,z	=	Rectangular coordinates
ε	=	Strain, mm/mm
σ	=	Stress, MPa
E	=	Modulus of elasticity, MPa
ν	=	Poisson's ratio
G	=	Shear modulus, MPa
V	=	Elastic strain energy of bending of a plate, N-mm
h	=	Thickness of plate, mm
D	=	$Eh^3/[12(1-\nu^2)]$, Bending stiffness or flexural rigidity of a plate, N-mm
ρ	=	Density, kg/mm^3
T	=	Kinetic energy of a vibrating plate, N-mm
ω	=	Angular frequency, radians/sec
λ	=	$\omega^2\rho ha^3b/D$, Characteristic value
a,b	=	Lateral dimensions of plate, mm
l	=	Length of beam, mm
$\left.\begin{matrix} m,n \\ i,k \\ p,q \\ r,s \end{matrix}\right\}$	=	Positive Integers
A_{mn}	=	A coefficient used in series representation of deflection
X_m	=	A function of x alone
Y_n	=	A function of y alone
φ_r	=	Characteristic function of a vibrating beam, as defined in [9]
α_r	=	Parameter in expressions for φ_r; values given in [9]
ε_r	=	Parameter in expressions for φ_r; values given in [9]
$\left.\begin{matrix} E_{mi}, F_{nk} \\ H_{im}, K_{kn} \end{matrix}\right\}$	=	Definite integrals defined by (16) through (18); values given in [9]
$C_{mn}^{(ik)}$	=	Coefficients defined by (15)
δ_{mn}	=	Kronecker delta

2.0 Introduction

2.1 Background

The Jet Propulsion Laboratory's (JPL) Mars Science Laboratory (MSL) mission will land a large robotic rover, named Curiosity, on to Mars in August 2012. Some of Curiosity's key science objectives involve performing in-situ chemistry and mineralogy experiments on samples collected from the surface and from within rocks using the onboard rotary-percussive drill. The suite of tools responsible for collecting, processing, and delivering these samples to the science instruments is the Sample Acquisition, Processing and Handling (SA/SPaH) subsystem. [7]

The Collection and Handling for In situ Martian Rock Analysis (CHIMRA) device, shown in Figure 1, is a component of SA/SPaH that is responsible for processing samples of soil and rock that have been collected. Within CHIMRA, the Primary Sieve, which is welded to the Primary Thwacker, shown in Figure 2, separates particles with a diameter smaller than 150 microns. [1] The Thwacker is vibrated, and particles that pass through the sieve may be delivered to other onboard instruments for analysis.

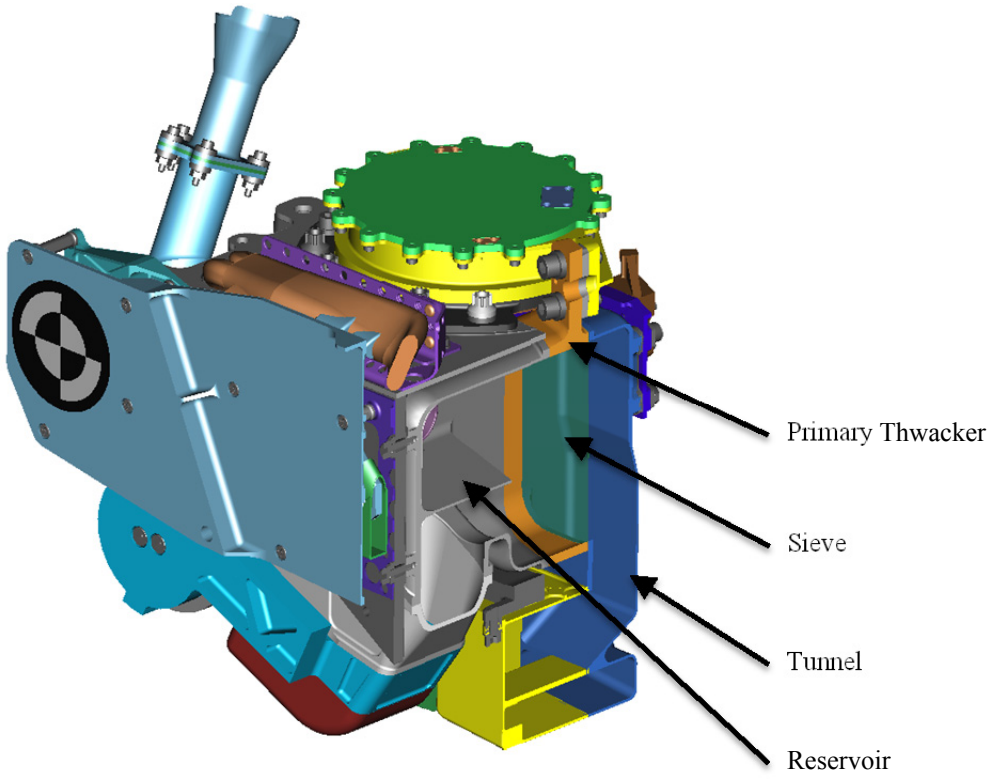

Figure 1. Section view of CHIMRA subsystem CAD model showing Primary Thwacker hardware

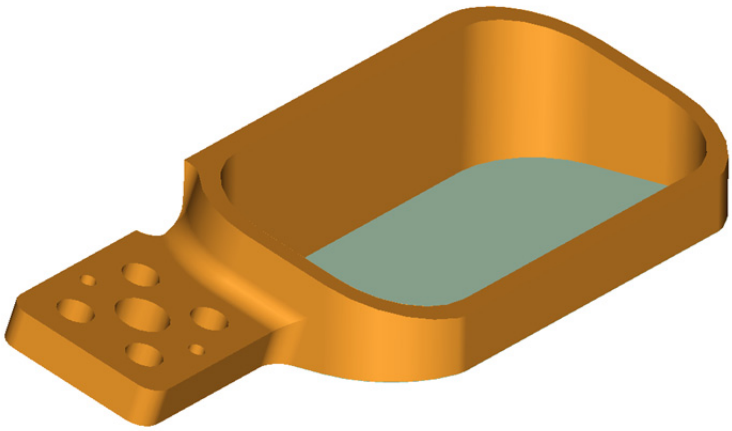

Figure 2. CAD model of Primary Thwacker Assembly

Thwacker frame is shown in brown, and sieve is shown in green.

At JPL, a series of testbeds were established to investigate the performance of the SA/SPaH subsystem, and to determine the appropriate procedures for collecting and processing different sample materials under environmental conditions analogous to those found on Mars. One testbed, the Qualification Model Dirty Test (QMDT) uses a Qualification Model version of the flight CHIMRA hardware. Another, the Challenge Materials Testbed (CMTB) only includes the primary sieve for processing samples. The design of the CMTB Thwacker, shown in Figure 3 and Figure 4, and its vibration hardware are similar to that of the flight hardware, but there are differences that may affect the way that it processes samples.

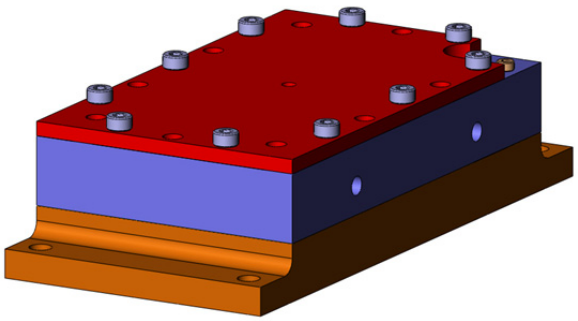

Figure 3. CAD model of CMTB Thwacker assembly

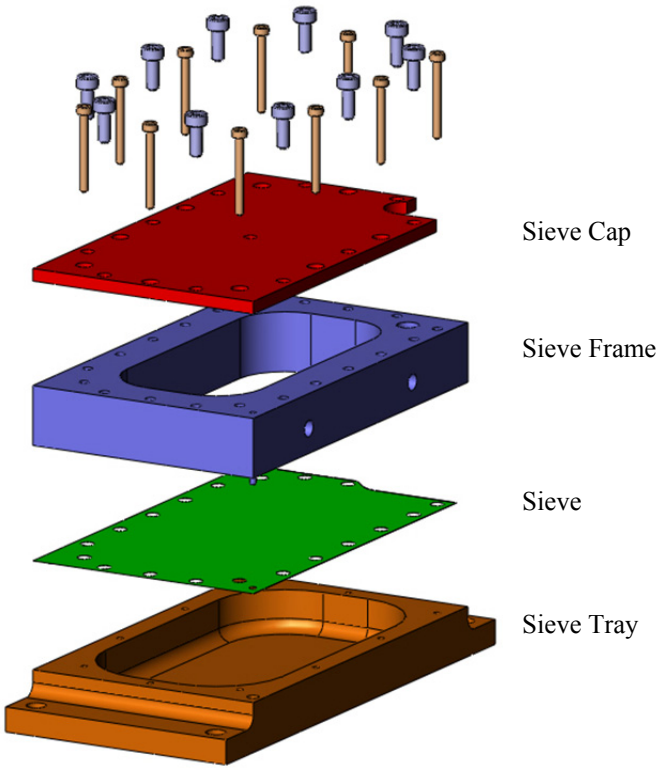

Figure 4. Exploded view of CMTB Thwacker Assembly CAD model

In both the Flight and CMTB Thwackers, the sieve is welded to the frame at discreet points with identical spacing. However, the frame of the CMTB Thwacker is significantly thicker than the Flight design. The Sieve Tray and Sieve Cap in the CMTB Thwacker take the place of the Reservoir and Tunnel in CHIMRA. While the Reservoir and Tunnel are preloaded against the Thwacker through a mechanism, the Tray and Cap are bolted directly to the Thwacker, resulting in much higher preload. Finally, while the Flight Thwacker is cantilevered from its support mechanism via a single flange, the CMTB Thwacker is attached through thicker flanges on both sides.

2.2 Problem Statement

The CMTB Thwacker hardware operates as an analogue for the Flight hardware that it is modeled after. The sieving behavior of the testbed hardware should be similar to the Flight hardware for the results to be meaningful. Since the performance of a sieve is governed by the dynamic interaction between the sample to be sieved and the sieve itself, it is important to understand the sieve's elastodynamic behavior. Knowledge of the dynamic behavior of the CMTB and Flight sieves can also be useful for predicting the optimal operating regimes for the hardware.

2.3 Objectives

The goal of this project is to analyze the Flight and CMTB Thwacker designs, and attempt to determine any significant differences. The elastodynamic behavior of the sieves will first be studied analytically using the Rayleigh Ritz method in conjunction with classical plate theory. Next, finite element models will be used to determine the mode shapes of both designs. A comparison between the natural frequencies and mode shapes will be made in order to recommend excitations for the testbed hardware that will most closely mimic the flight hardware. Finally, the effects of a sample on the mode shapes of the sieve will be investigated.

3.0 Analysis

3.1 Effective Material Properties Generation

In order to determine the natural frequencies of the sieve systems, a finite element mesh must be generated. If the hole features in the actual sieve were to be modeled, their small size would require an extremely fine mesh, and a prohibitively large number of elements. One method to reduce the complexity of the sieve is to model it as a homogenous solid without holes, but with effective material properties that match the actual bulk material.

So long as deflections are small, Timoshenko has shown that the vibration response of an elastic, homogenous, and isotropic plate with uniform thickness is only dependent on its stiffness, E, Poisson ratio, ν, and density, ρ. [8] If the geometry and boundary conditions meet certain criteria, effective properties may be measured using a unit cell approach. [5] A schematic of the sieve mesh is shown in Figure 5. The mesh geometry contains repetitive elements, which allows for selection of a periodic element such as the shaded area ‘A’. When bulk material stresses are applied to the element, the effective stiffness may be determined by dividing the magnitude of the stress by the resulting strain. The effective Poisson ratio is determined by the ratio of strains in orthogonal directions. The effective density is the ratio of the element’s area that is occupied by material to its total boundary area, multiplied by the bulk density.

In general, if the entire periodic element geometry is used for analysis, the constraints at the element’s boundaries must take the form of periodic boundary conditions. However, under symmetric loading conditions, additional symmetries in the geometry allow the periodic element to be further subdivided in to a unit cell represented by the shaded area ‘B1’. [5]

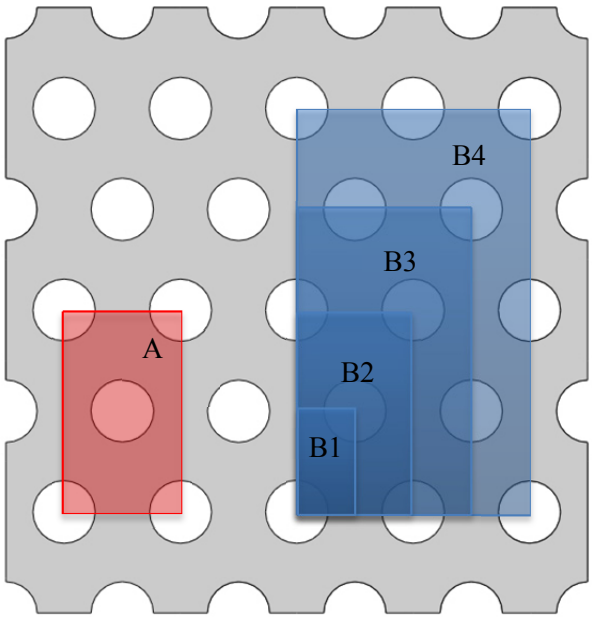

Figure 5. Possibilities for sieve mesh periodic elements.

B1 represents the smallest unit cell available if only symmetric boundary conditions are applied. B2 through B4 represent 1X1, 2X2, etc. multiples of the unit cell.

A finite element model of the unit cell, created using 10-node tetragonal solid elements is shown in Figure 6. The bulk material of the sieve is Grade 4 commercially pure titanium. The properties for this material, along with the Ti-6Al-4V that is used in other elements of the Primary Thwacker hardware are listed in Table 1. Symmetry conditions were applied to the faces along the planes X=0 and Y=0, and Z=0 as shown in Figure 7 and the thickness of the part in the Z direction is equal to half of the sieve thickness.

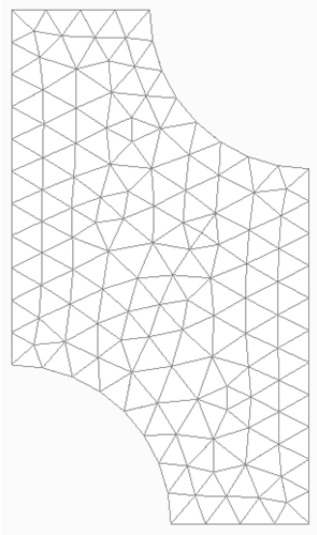

Figure 6. Finite element mesh of Sieve unit cell

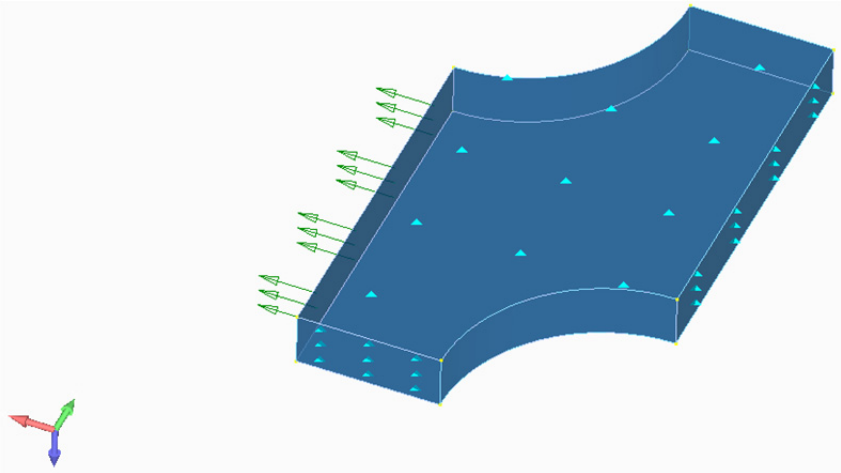

Figure 7. Loads and constraints applied to unit cell FEM.

Table 1. Material Properties used in components of Primary Thwacker and Sieve Assemblies

	Titanium, CP-4, [3],[4]	Ti-6Al-4V [4]
Density, ρ, kg/mm^3	4.51x10^{-6}	4.43x10^{-6}
Modulus of Elasticity, E, GPa	106.9	110.3
Poisson's Ratio, ν	0.361	0.31

A distributed force, equivalent to a bulk stress of 1 MPa was applied to each of the free faces, one at a time, and the displacements of the faces were measured using RBE3 interpolation elements. The stiffness was calculated by dividing the bulk stress by the measured strain. The effective modulus of elasticity was calculated using the average of the stiffnesses in the *x* and y directions. The Poisson's ratio was calculated by dividing the lateral strains. The effective Poisson's ratio was calculated by averaging the *x* and *y* results. The bulk material density was multiplied by the ratio of the material area to the unit cell area to determine the effective density. The analysis was repeated with four additional models: B2, B3, B4, and B8; each model increased the size the unit cell to capture additional holes, while retaining the symmetry conditions. The effective material properties for these analyses are plotted with respect to the unit cell area in Figure 8 and Figure 9. The properties determined for B8 were assumed to be the effective properties of the sieve.

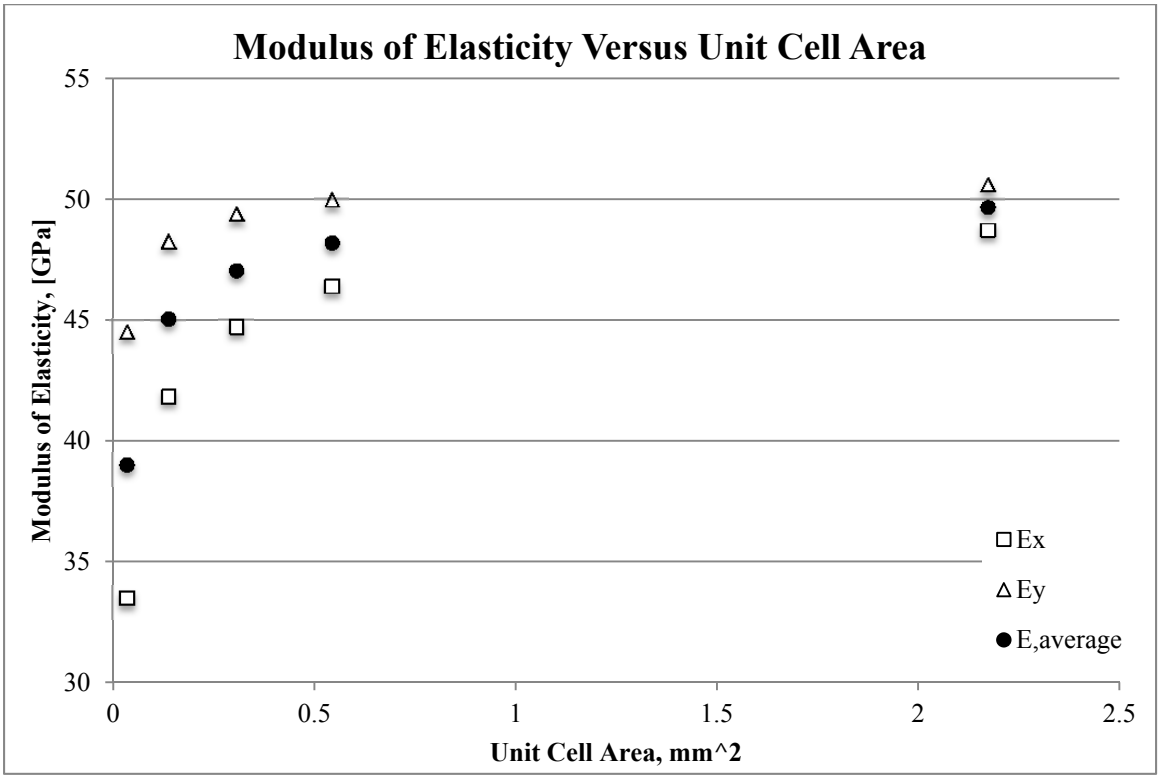

Figure 8. Modulus of Elasticity with respect to unit cell area

Results are shown for the unit cells B1, B2, B3, B4, and B8.

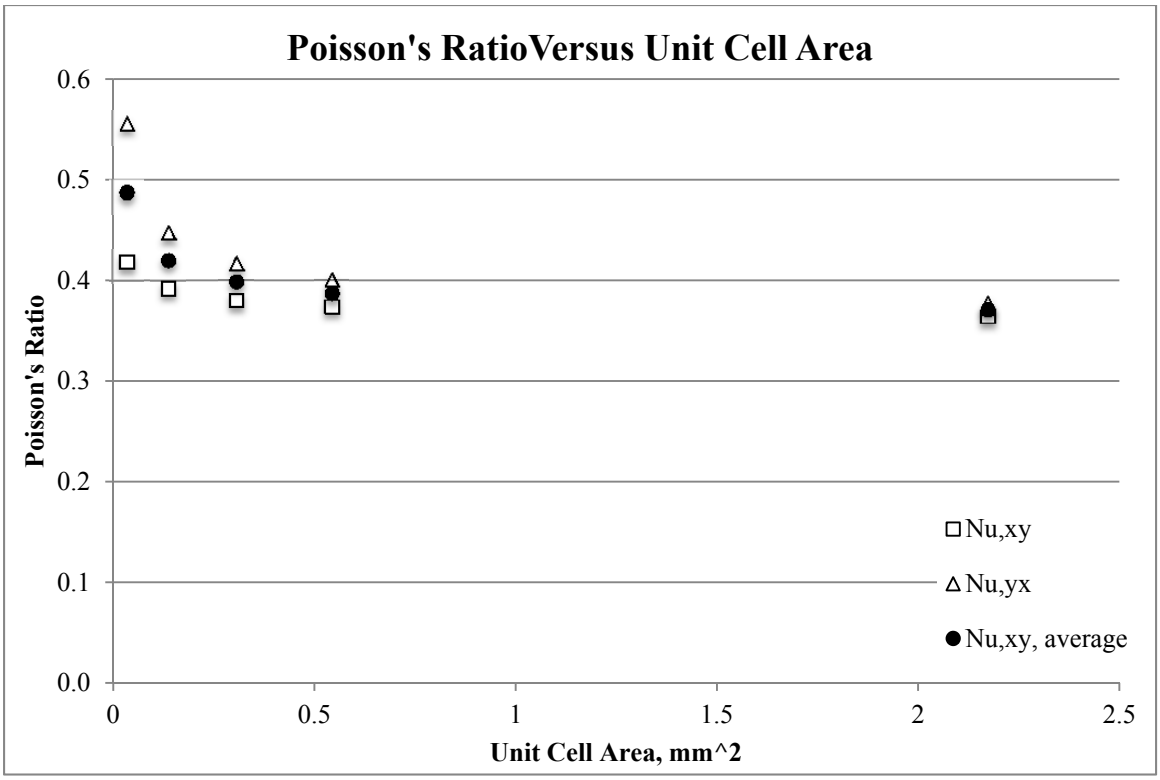

Figure 9. Poisson's Ratio with respect to unit cell area.

Results are shown for the unit cells B1, B2, B3, B4, and B8.

When a collected sample is introduced on to the sieve, the interaction between the sample and the sieve changes its dynamic response. For the purpose of this analysis, the sample material is assumed to be spread evenly over the sieve, and physically bonded to it. Hence, the sample effectively increases the density of the sieve material. Prior testing has shown that a reasonable collection limit is 30 grams. This mass, when spread over the exposed sieve area, effectively increases its material density by 2.041×10^{-4} kg/mm^3. Table 2 summarizes the sieve material properties, with and without sample, that are used for the following analysis.

Table 2. Sieve bulk and effective material properties, with and without sample

	Bulk Material		Effective Material	
	Without Sample	With Sample	Without Sample	With Sample
Density, ρ, kg/mm^3	4.51×10^{-6}	2.086×10^{-4}	3.34×10^{-6}	2.074×10^{-4}
Modulus of Elasticity, E, GPa	106.9	106.9	49.67	49.67
Poisson Ratio, ν	0.361	0.361	0.371	0.371

3.2 Analytical Model Predictions

Lord Rayleigh first demonstrated a method for determining the approximate natural vibration mode shapes and corresponding characteristic frequencies for a plate. [6] Timoshenko further elaborated on the method for an elastic, homogenous, and isotropic material with uniform thickness. [8] The strains in the *x* and *y* directions that are caused by a deflection normal to the *z* axis, *w(x,y)*, may be expressed as follows,

$$\left.\begin{aligned} \epsilon_{xx} &= -z\frac{\partial^2 w}{\partial x^2} \\ \epsilon_{yy} &= -z\frac{\partial^2 w}{\partial y^2} \\ \epsilon_{xy} &= -2z\frac{\partial^2 w}{\partial x \partial y} \end{aligned}\right\} \quad (1)$$

with corresponding stresses,

$$\left.\begin{aligned} \sigma_{xx} &= \frac{E}{1-\nu^2}\left(\epsilon_{xx}+\nu\epsilon_{yy}\right) = -\frac{Ez}{1-\nu^2}\left(\frac{\partial^2 w}{\partial x^2}+\nu\frac{\partial^2 w}{\partial y^2}\right) \\ \sigma_{yy} &= \frac{E}{1-\nu^2}\left(\epsilon_{yy}+\nu\epsilon_{xx}\right) = -\frac{Ez}{1-\nu^2}\left(\frac{\partial^2 w}{\partial y^2}+\nu\frac{\partial^2 w}{\partial x^2}\right) \\ \sigma_{xy} &= G\epsilon_{xy} = -\frac{Ez}{1+\nu}\cdot\frac{\partial^2 w}{\partial x \partial y} \end{aligned}\right\} \quad (2)$$

The potential energy generated by the deformation of a differential element of the plate will be,

$$dV = \left(\frac{\epsilon_{xx}\sigma_{xx}}{2}+\frac{\epsilon_{yy}\sigma_{yy}}{2}+\frac{\epsilon_{xy}\sigma_{xy}}{2}\right)dxdydz$$

$$dV = \frac{Ez^2}{2(1-\nu^2)}\left\{\left(\frac{\partial^2 w}{\partial x^2}\right)^2+\left(\frac{\partial^2 w}{\partial y^2}\right)^2+2\nu\frac{\partial^2 w}{\partial x^2}\frac{\partial^2 w}{\partial y^2}+2(1-\nu)\left(\frac{\partial^2 w}{\partial x \partial y}\right)^2\right\}dxdydz \quad (3)$$

Integrating the potential energy of bending, (3), over the entire plate yields,

$$\begin{aligned} V = \iiint dV = \frac{D}{2}\iint\Bigg\{&\left(\frac{\partial^2 w}{\partial x^2}\right)^2+\left(\frac{\partial^2 w}{\partial y^2}\right)^2+2\nu\frac{\partial^2 w}{\partial x^2}\frac{\partial^2 w}{\partial y^2} \\ &+2(1-\nu)\left(\frac{\partial^2 w}{\partial x \partial y}\right)^2\Bigg\}dxdy \end{aligned} \quad (4)$$

Where $D = \frac{Eh^3}{12(1-\nu^2)}$ is the flexural rigidity of the plate. The kinetic energy of the vibrating plate will be:

$$T = \frac{\rho h}{2} \iint \dot{w}^2 dxdy \quad (5)$$

If the deflection of the plate is assumed to take the form,

$$w(x, y, t) = w_0(x, y) \cos \omega t \quad (6)$$

where $w_0(x, y)$ is an approximation of the deflection $w(x, y)$, made up of a series of admissible shape functions X(x)Y(y) multiplied by weight coefficients A_{mn}:

$$w_0(x, y) = \sum_{m=1}^{p} \sum_{n=1}^{q} A_{mn} X(x) \cdot Y(y) \quad (7)$$

then the maximum potential and kinetic energies may be rewritten as,

$$V_{max} = \frac{D}{2} \iint \left\{ \left(\frac{\partial^2 w_0}{\partial x^2} \right)^2 + \left(\frac{\partial^2 w_0}{\partial y^2} \right)^2 + 2\nu \frac{\partial^2 w_0}{\partial x^2} \frac{\partial^2 w_0}{\partial y^2} + 2(1-\nu) \left(\frac{\partial^2 w_0}{\partial x \partial y} \right)^2 \right\} dxdy \quad (8)$$

$$T_{max} = \frac{\rho h \omega^2}{2} \iint {w_0}^2 dxdy \quad (9)$$

By equating (8) and (9),

$$\omega^2 = \frac{2}{\rho h \omega^2} \frac{V_{max}}{\iint {w_0}^2 dxdy} \quad (10)$$

The natural frequencies of the plate are the solutions that minimize (10). These solutions may be found by taking the partial derivatives of (10) with respect to the weight coefficients, and setting the result equal to zero:

$$\frac{\partial V}{\partial A_{ik}} - \frac{\rho h \omega^2}{2} \frac{\partial}{\partial A_{ik}} \iint {w_0}^2 dxdy = 0 \quad (11)$$

Young proposed a set of characteristic functions for the displacement of a plate. [9] The particular functions used for X(x) and Y(y) depend on the types of constraints in each direction. For the purpose of this analysis, the characteristic functions for the rth mode of a clamped-clamped beam,

$$\varphi_r = \cosh\frac{\epsilon_r x}{l} - \cos\frac{\epsilon_r x}{l} - \alpha_r\left(\sinh\frac{\epsilon_r x}{l} - \sin\frac{\epsilon_r x}{l}\right) \quad (12)$$

were chosen for both directions. Each member of the set of characteristic functions corresponds to an integer value of r, and is orthogonal with respect to the other members of the set. Young calculated specific values of ϵ_r and α_r for various choices or r.

By making use of (7), (8), (12), and the orthogonality of the characteristic functions, the set of equations given in (11) may be reduced to form

$$\sum_{m=1}^{p}\sum_{n=1}^{q}\left[C_{mn}^{(ik)} - \lambda\delta_{mn}\right]A_{mn} = 0 \quad (13)$$

Where,

$$\lambda = \frac{\omega^2\rho h a^3 b}{D} \quad (14)$$

$$\begin{cases} C_{mn}^{(ik)} = \upsilon\frac{a}{b}[E_{mi}F_{kn} + E_{im}F_{nk}] + 2(1-\upsilon)\frac{a}{b}H_{im}K_{kn} \dots\dots\dots\dots\dots mn \neq ik \\ C_{mn}^{(ik)} = \frac{b}{a}\epsilon_i^4 + \left(\frac{a}{b}\right)^3\epsilon_k^4 + 2\upsilon\frac{a}{b}E_{ii}F_{kk} + 2(1-\upsilon)\frac{a}{b}H_{ii}K_{kk} \dots\dots\dots\dots mn = ik \end{cases} \quad (15)$$

$$E_{im} = a\int_0^a X_i\frac{d^2X_m}{dx^2}dx\ ,\ E_{mi} = a\int_0^a X_m\frac{d^2X_i}{dx^2}dx \quad (16)$$

$$F_{kn} = b\int_0^b Y_k\frac{d^2Y_n}{dy^2}dy\ ,\ F_{nk} = b\int_0^b Y_n\frac{d^2Y_k}{dy^2}dy \quad (17)$$

$$H_{im} = a\int_0^a \frac{dX_i}{dx}\frac{dX_m}{dx}dx\ ,\ K_{kn} = b\int_0^b \frac{dY_k}{dy}\frac{dY_n}{dy}dy \quad (18)$$

The values for (16) through (18) as well as ϵ were calculated by Young and have not been included here. There will be one equation of type (13) for each of the $p*q$ combinations of ik, and the characteristic values λ are determined by setting the determinant of these equations equal to zero.

An analysis was performed using MATLAB to solve for the natural frequencies of a rectangular plate using the method described above. The analysis was first checked against the results

published by Young for a clamped square plate, and the normalized natural frequencies were found to agree. Next, the first six natural frequencies were determined for a clamped plate with the geometry and material properties of the sieve. The plate dimensions a and b corresponded to the size of the sieve pocket, and thus any effects of the corner radii were ignored. Two analyses were performed: one with material properties corresponding to the bulk sieve listed Table 1, and the other with sample-free properties of the effective sieve materials listed in Table 2. The results for the two sieve materials are plotted in Figure 10 below.

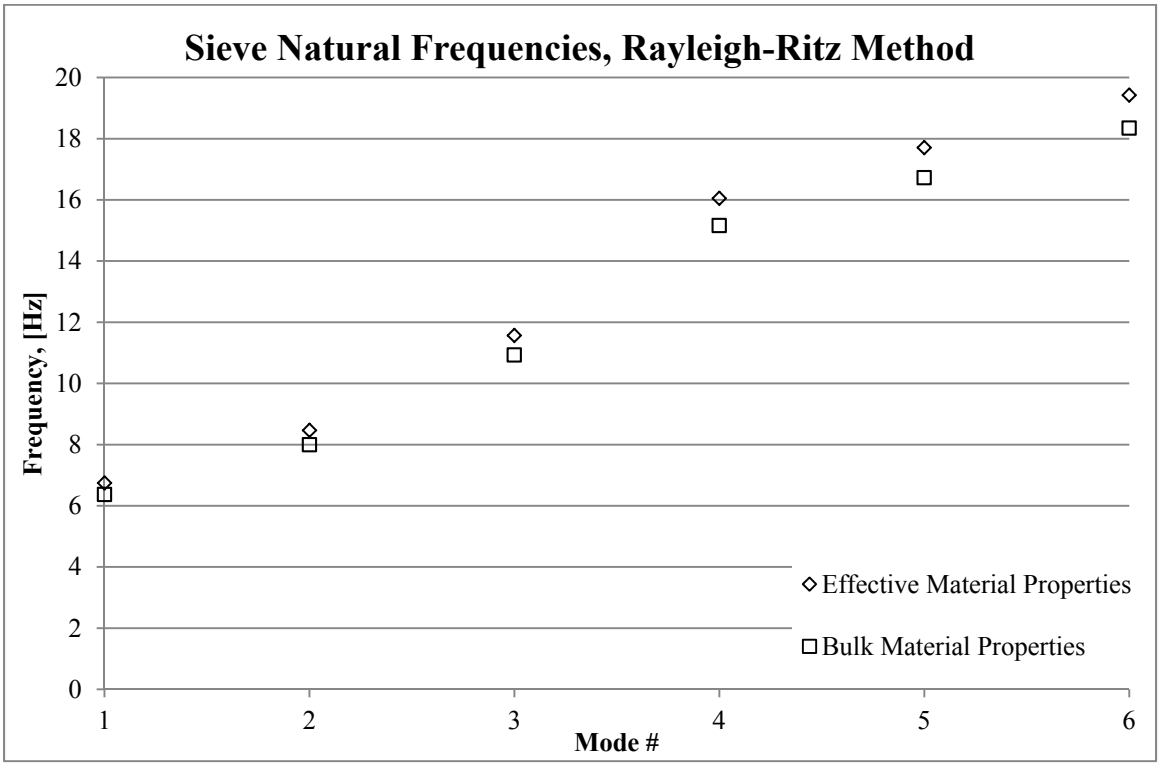

Figure 10. Comparison of first six natural frequencies for effective and bulk sieve material properties, using Raleigh-Ritz method.

3.3 Finite Element Modal Analysis

A series of finite element models were generated to accomplish the objectives of this analysis. First, a finite element model of the sieve geometry was created to determine the eigenmodes and natural frequencies the sieve alone. These frequencies were compared with the frequencies estimated using the Raleigh-Ritz method in Section 3.2. Next, finite element models of the Flight and CMTB Thwackers were constructed. Modal analysis of both models allows for direct comparison of the two designs. All models were generated using Femap 10.3.1, and all solutions were generated using MSC Nastran 2012.1.

3.3.1 Sieve Only

The dimensions of the sieve geometry are the same as the inside pocket of the Primary and CMTB Thwacker frames. The finite element mesh, made up of eight-node quadrilateral (CQUAD8) and six-node triangular (CTRIA6) plate elements, is shown in Figure 11 below. The element size along the perimeter of the geometry was chosen to match the spacing of the weld joints that secure the sieve to frame. The boundary between the red and blue elements shown in Figure 11 represents the diameter of the perforated portion of the sieve. The bulk material properties from Table 2 were applied to the red elements, and effective properties were applied to the blue elements.

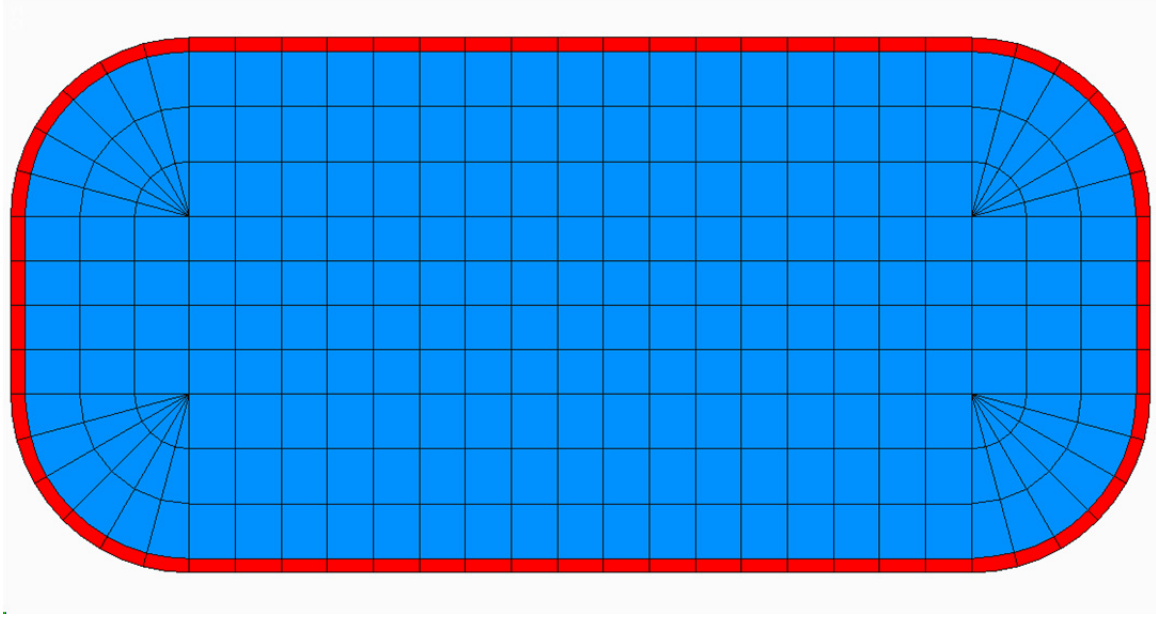

Figure 11. Finite element model of sieve

Elements with bulk material properties are shown in red, those with effective material properties are shown in blue.

In both the Testbed and Primary Thwacker designs, the sieve is welded to a frame and clamped between the frame and additional hardware. The welds constrain in-plane deformation, and the clamping constrains out-of-plane bending. In order to mimic these conditions, fixed boundary constraints were applied to the outer boundary of the sieve.

Several normal mode eigenvalue analyses were performed to determine the natural frequencies of the sieve between 0 and 100 Hz with varying amounts of sample present. The results of these analyses are presented in Figure 12; the horizontal and vertical origins have been swapped for this plot. The results for the sieve without sample are shown in greater detail in Figure 13.

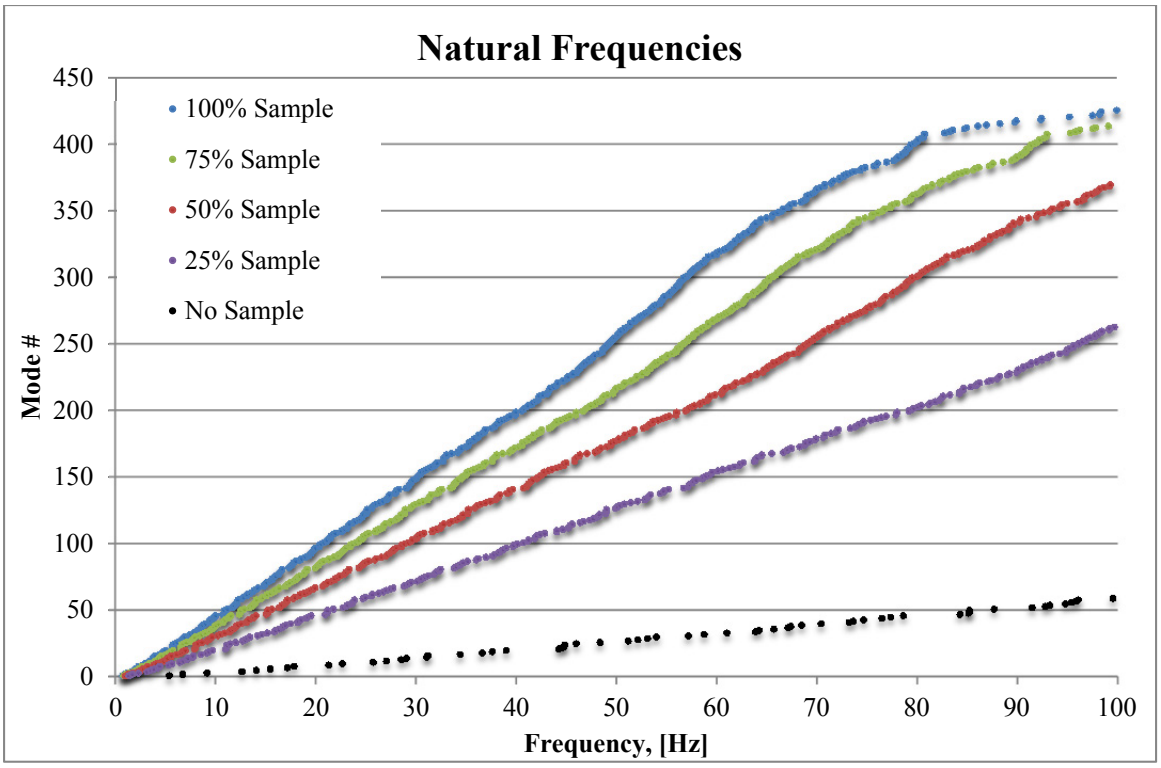

Figure 12. Natural frequencies of sieve with varying percentages of maximum sample.

In this chart frequency has been plotted along the horizontal rather than the vertical ordinate for clarity.

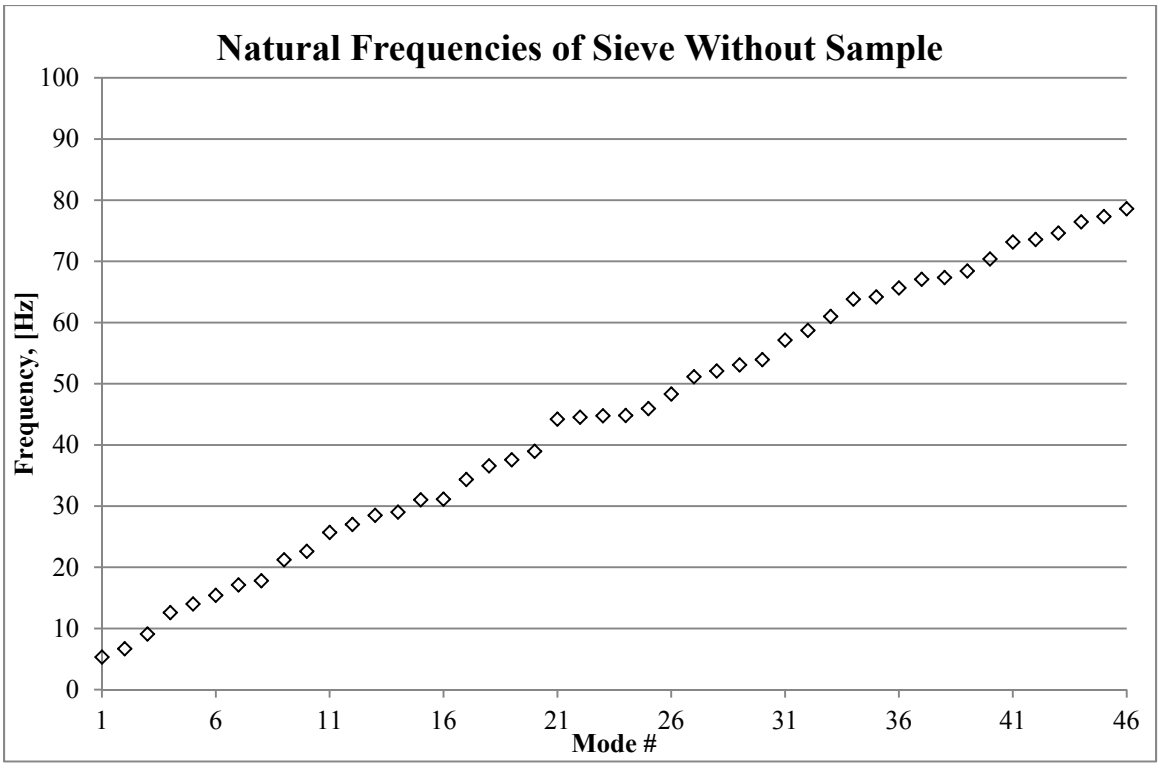

Figure 13. Natural frequencies of sieve with no sample

3.3.2 Flight Hardware Design

The finite element mesh of the Primary Thwacker Frame was generated using the CAD model shown in Figure 2 with no simplification. The mesh was made up of ten-node tetragonal (CTETRA) solid elements, and is highlighted gold in Figure 14. The element size along the perimeter of sieve pocket was chosen to match the spacing of the weld joints that secure the Sieve to the Frame. The frame elements were assigned material properties for Ti-6Al-4V listed in Table 1.

The finite element mesh of the Sieve is identical to the one presented in Section 3.3.1, with the exception of a ring of eight-node quadrilateral (CQUAD) plate elements, highlighted green in Figure 14, that have been added around the perimeter of the sieve. These elements were assigned the bulk material properties from Table 2. A connection between the mesh and frame elements is formed by merging nodes of the green elements with those on the top face of the frame. Only the corner nodes of the sieve elements, highlighted in Figure 15 were merged. Merging nodes along both the inner and outer edges of the frame was necessary to maintain continuity between the solid elements, whose nodes only support deflection, and the plate elements whose nodes support both deflection and rotation. Merging the nodes allows deformation of the frame to transmit both membrane and bending loads in to the sieve, and vice-versa.

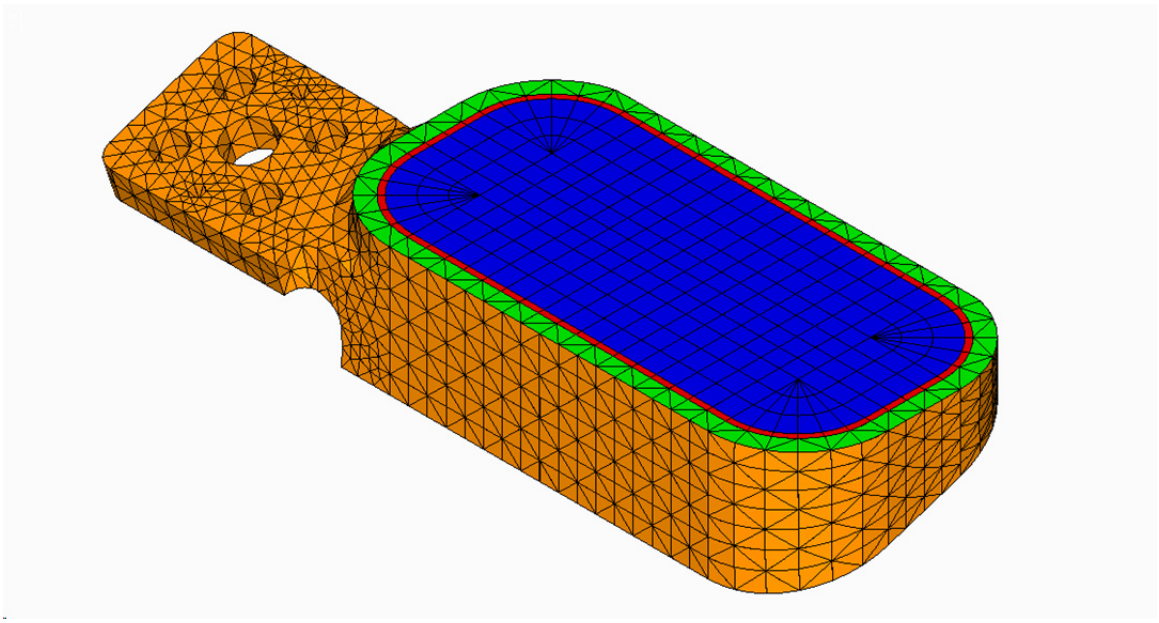

Figure 14. Finite element model of Primary Thwacker

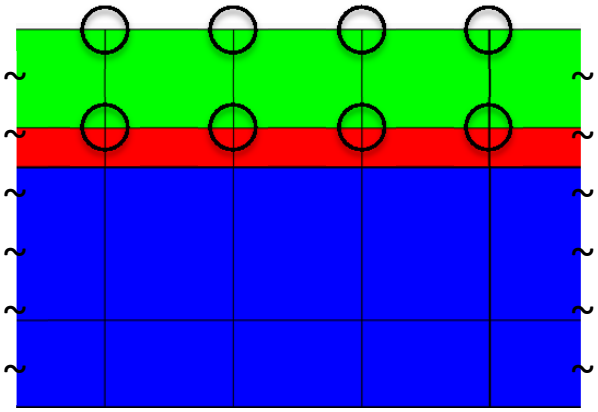

Figure 15. Typical nodes that were merged between sieve and frame elements

The finite element mesh was constrained via four rigid elements (RBE2) centered in the clearance holes of the frame. For each element, the nodes along the top edge of a hole were dependent, and a central independent node was pinned. This constraint fixed the three translational degrees of freedom at each hole, but left the three rotational degrees of freedom unconstrained. The arrangement, shown in Figure 16 mimics the four fasteners that secure the frame to the Thwacker Mechanism.

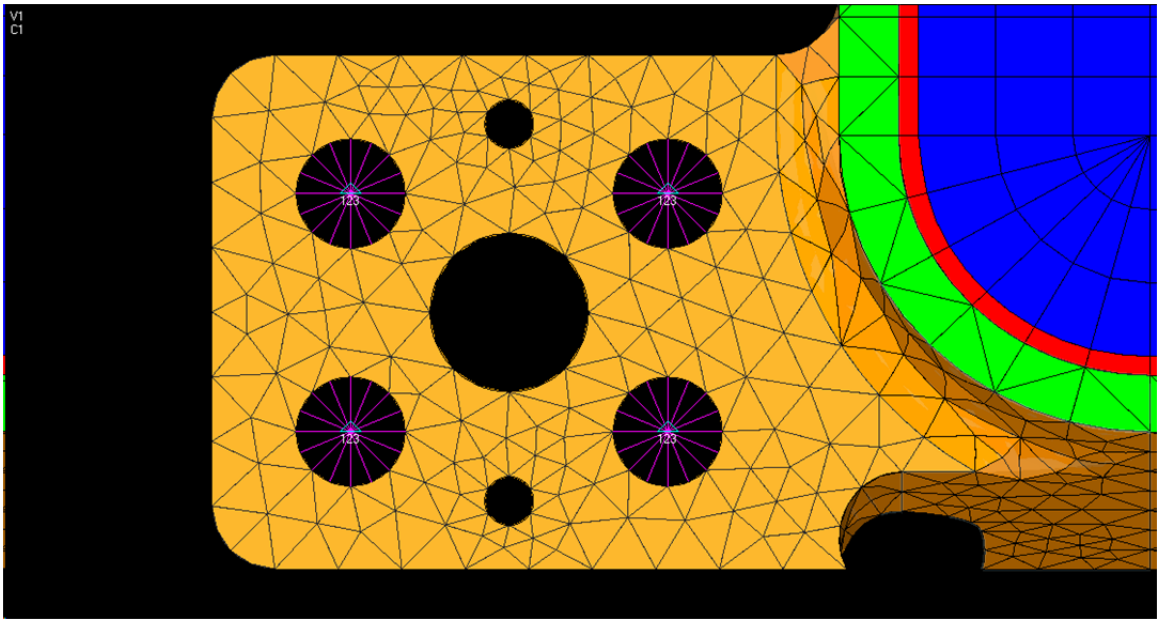

Figure 16. Rigid elements used to constrain the Primary Thwacker Frame

A normal mode eigenvalue analysis was performed to determine the natural frequencies of the Primary Thwacker between 0 and 100 Hz, without sample present. For the majority of the normal modes, the Thwacker Frame's deformation was minimal when compared to the sieve deformation. For those modes in which the Frame's contribution was significant, the shapes of the deformed meshes are shown in Figure 17. The natural frequencies for the analyses are presented in Figure 18, with the Frame modes highlighted in red.

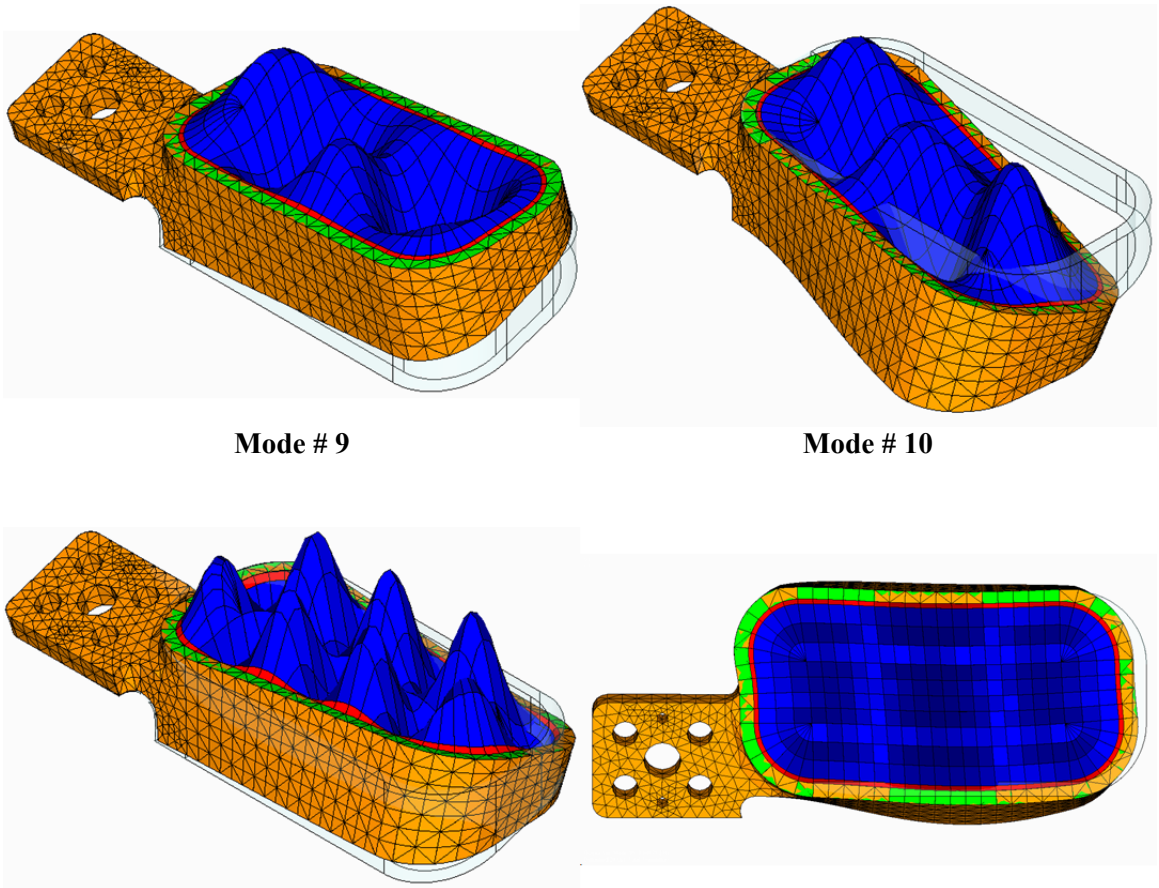

Mode # 9 **Mode # 10**

Mode # 23 **Mode # 59**

Figure 17. Mode Shapes of Primary Thwacker Frame

Deformations have been scaled to 10% of model size.

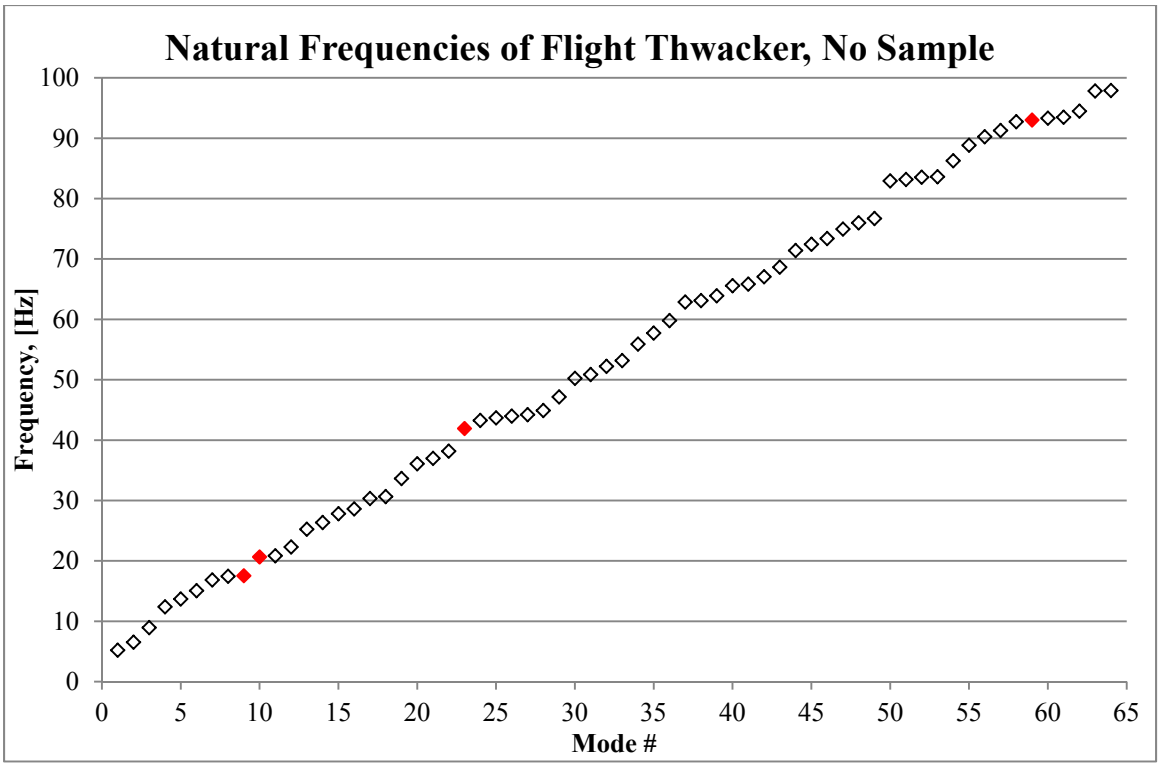

Figure 18. Natural frequencies of the Primary Thwacker without sample

Thwacker Frame modes are highlighted in red.

3.3.3 CMTB Hardware Design

The finite element meshes of the CMTB Thwacker Frame, Tray and Lid were generated using the CAD model shown in Figure 3. All fasteners were removed, and the models were simplified to remove all holes except for the four on the flanges of the Tray. The meshes, composed of ten-node tetragonal (CTETRA) solid elements, are shown Figure 19. The elements were assigned the material properties for Ti-6Al-4V listed in Table 1. The element size along the perimeter of sieve pocket was chosen to match the spacing of the weld joints that secure the sieve to the frame.

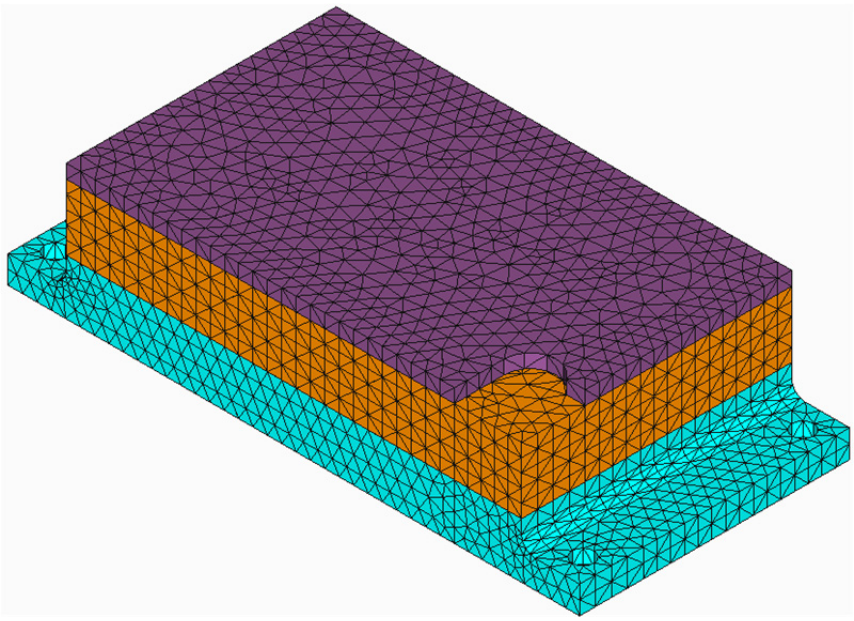

Figure 19. Finite element model of CMTB Thwacker Assembly

Lid, Frame, and Tray elements are highlighted in purple, gold, and cyan, respectively.

Both the finite element mesh of the Sieve, and its method of constraint are identical to the description presented in Section 3.3.2. The mesh of the Sieve is shown in Figure 20. The tray mesh was constrained via four rigid elements (RBE2) centered in the clearance holes of the tray. For each element, the nodes along the top edge of a hole were dependent, and a central independent node was pinned. The arrangement, shown in Figure 21 mimics the four fasteners that secure the Tray to its support hardware.

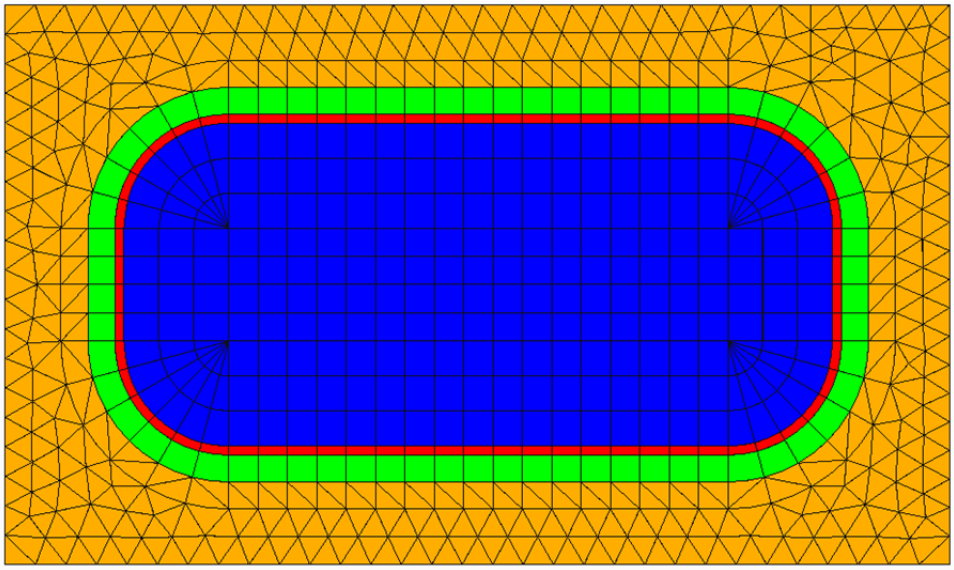

Figure 20. Bottom view of the CMTB Thwacker Assembly.

The Tray elements have been hidden to reveal the mesh of Sieve elements.

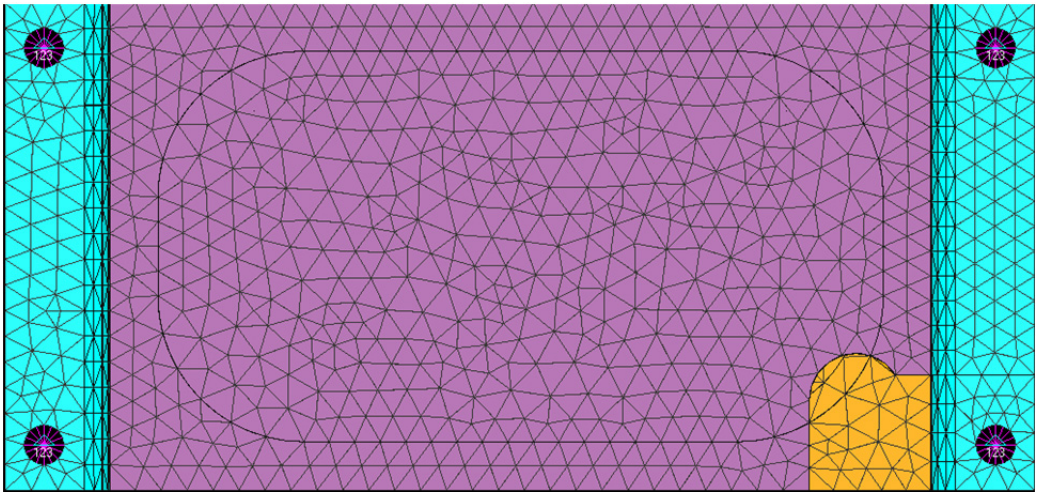

Figure 21. Rigid elements used to constrain the CMTB Thwacker Assembly

A normal mode eigenvalue analysis was performed to determine the natural frequencies of the CMTB Thwacker Assembly between 0 and 100 Hz, without sample present. For the majority of the normal modes, the deformations of the structural component (Lid, Frame, Tray) were minimal when compared to the sieve deformation. For those modes in which the structural component contributions were significant, the shapes of the deformed meshes are shown in Figure 22. The natural frequencies for the analyses are presented in Figure 23, with the structural component's modes highlighted in red.

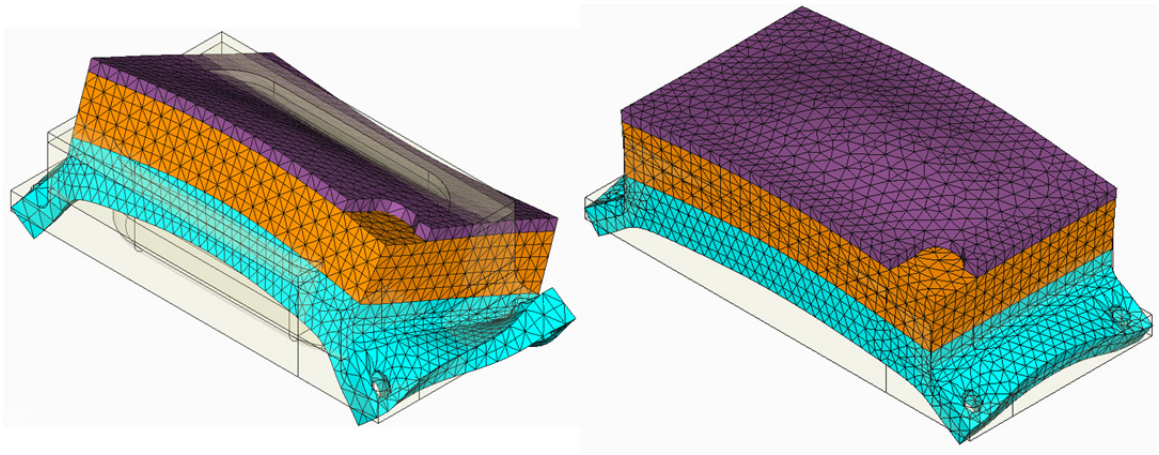

Mode # 55 **Mode # 60**

Figure 22. Structure mode shapes of CMTB Thwacker Assembly.

Deformations have been scaled to 10% of model size.

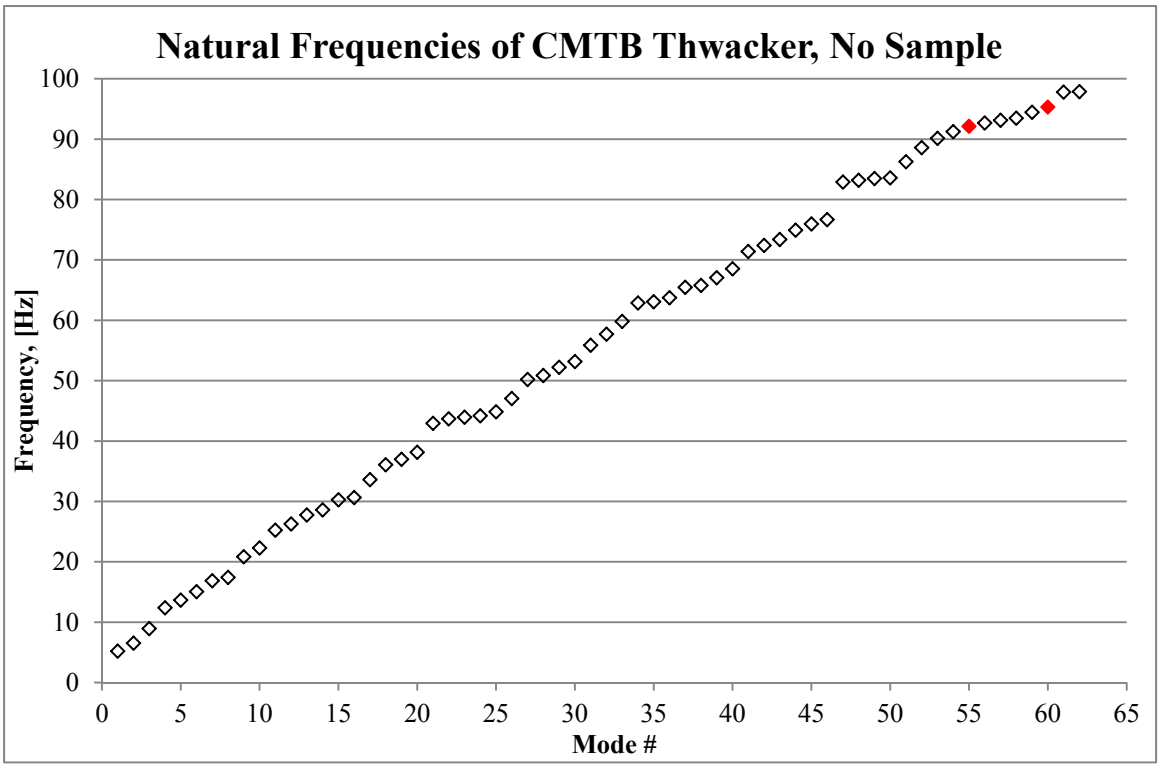

Figure 23. Natural frequencies of the CMTB Thwacker Assembly without sample.

Structural component modes are highlighted in red.

4.0 Discussion

Effective Material Properties Generation

The benefit of using a unit cell analysis to determine effective material properties is that the properties can be determined from a simple model that requires little processing time. If, for example, the entire sieve with holes was meshed, the number of elements would prohibit finding a solution with a consumer grade computer. The success of unit cell analysis, however, is dependent on the degree to which the boundary conditions mimic the mechanics of the problem. [5]

With proper boundary conditions, the results from a unit cell analysis should be scalable to any size and yield the same results. The asymptotic behavior of the effective material properties shown in Figure 8 and Figure 9 suggest that this was not the case. However, with a sufficiently large portion of the sieve modeled, the results should be satisfactorily close to the exact solution. If the periodic boundary conditions were applied to the model the results would improve. These type of constraints were not easy to produce with the Femap FEM package.

Additionally, depending on the level of fidelity and frequency range desired in the modal response, effective property generation may not be required. As shown in Figure 10 for the first six modes, the difference between the response using effective and bulk properties is less than 26%.

Comparison of Modal Analysis Techniques

Although it is possible to apply the Rayleigh-Ritz technique to determine natural frequencies above the sixth mode, this method should be used with caution. The method assumes classical plate theory with small deformations of the sieve. For higher modes, the curvature of the surface increases, and the quality of the approximation will decrease. However, for the frequency domain considered in this analysis, this method appears to provide a good approximation.

As shown in Figure 24, the results from the Raleigh-Ritz method track very well with those determined using finite element analysis. The Raleigh-Ritz solution tends to yield a lower natural frequency for each mode, and the difference between the results and those determined with FEA tends to increase with frequency. Theoretically, the Raleigh-Ritz solution should always provide an upper limit to the natural frequency. [9] The reduced stiffness can most likely be attributed to the fact that a square plate was assumed for the Raleigh-Ritz analysis, while the corners of the sieve were actually rounded. As a plate's area is increased, its natural frequency tends to decrease.

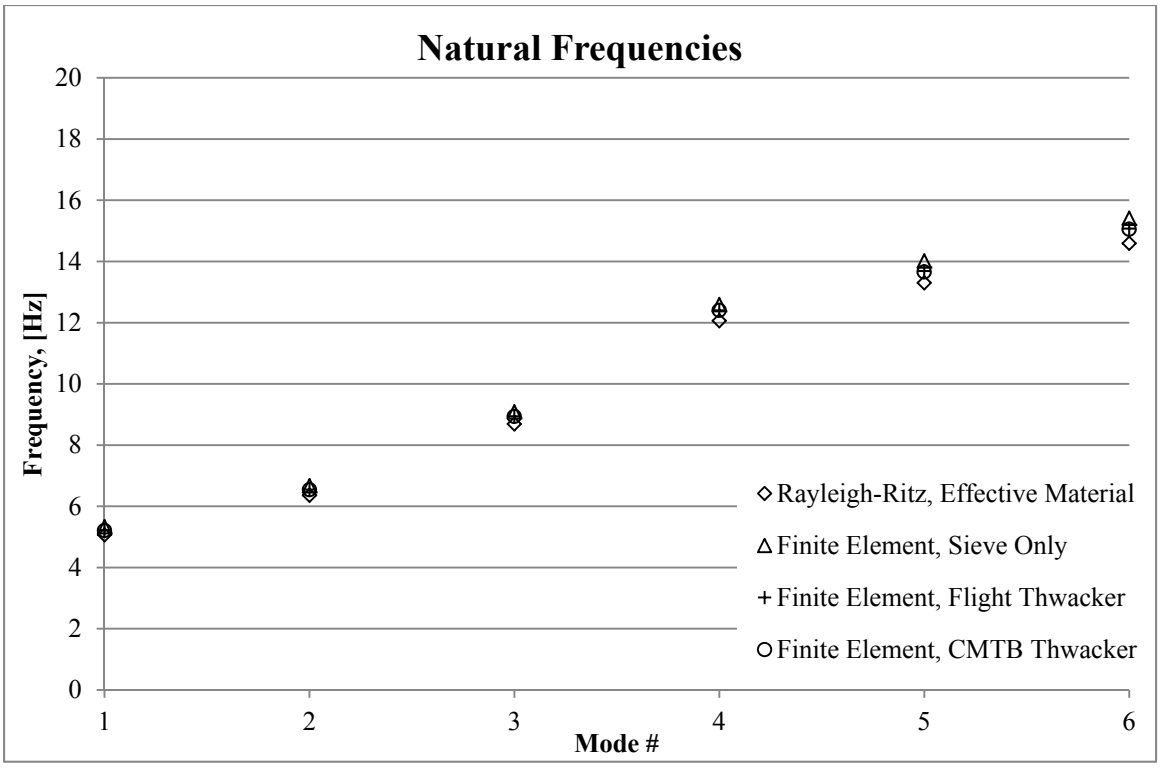

Figure 24. Comparison of sieve natural frequencies determined using different analysis techniques

Comparison of Natural Frequencies Among Hardware Designs

A comparison of the natural frequencies for the Flight, CMTB and bare sieve designs is shown in Figure 25. The natural frequencies for each mode of the different configurations are not the same. The Flight and CMTB sieves have structural modes unique to each other that are not present for the model of the sieve alone. Additionally, the clamped constraint around the edge of the sieve-only model is significantly stiffer than the welded joint to the frame in the two other configurations. This increased stiffness probably caused the sieve-only modes to consistently shift toward higher frequencies.

It may also be observed that, except for the structural modes unique to the CMTB and Testbed configurations, the modal response for the two designs is very similar. For each natural frequency of the Flight Thwacker, a lower mode is present for the CMTB Thwacker at nearly the same frequency. This pattern is likely present because the majority of the modal responses are determined by the sieve itself. Since the sieve geometry and mounting method for both configurations was assumed to be the same, the responses are very similar.

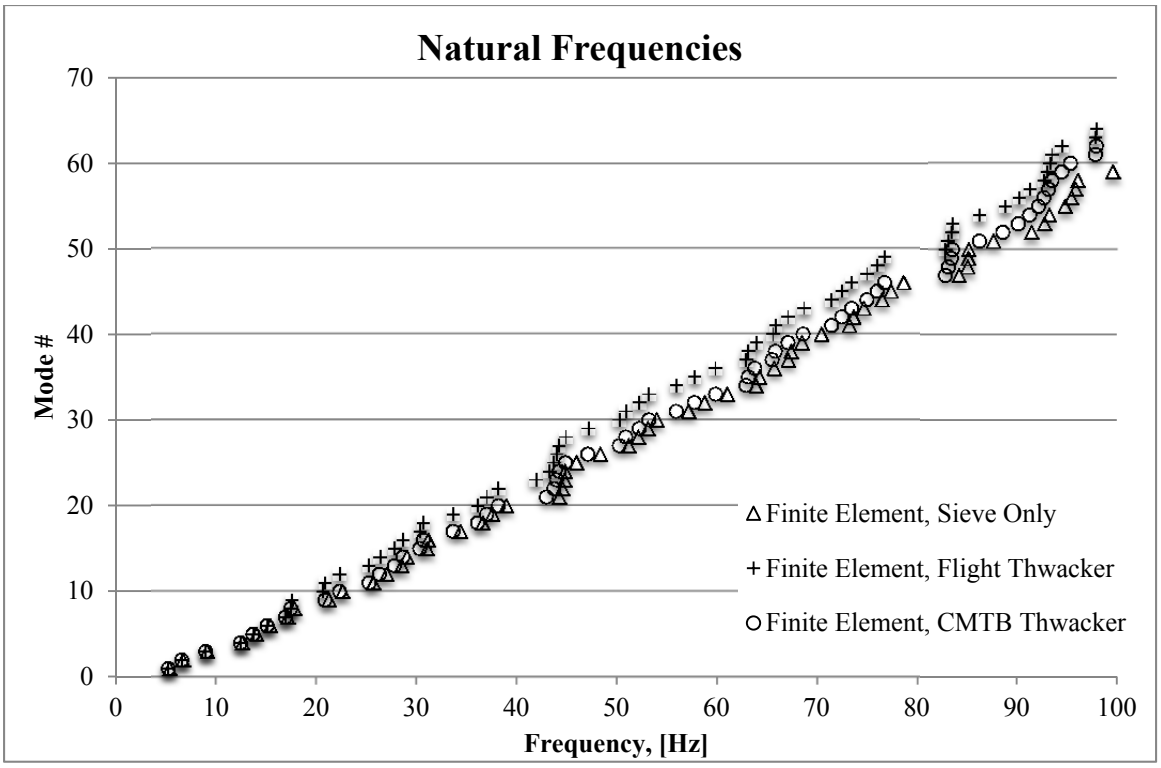

Figure 25. Comparison of natural frequencies among sieve hardware designs

In reality, the responses of the two configurations may not be as similar as suggested by Figure 25. The Flight Thwacker model was fixed on the flange, and allowed to cantilever. The actual hardware is attached to the Thwacker mechanism, which would provide a softer support, lowering the natural frequencies of the structural modes. However, the Flight Thwacker is also restrained between the preloaded Tunnel and Reservoir, which would tend to increase the stiffness of the cantilevered portion. The effects of these configuration changes on the modal response are impossible to accurately predict without significantly more complex models.

The same may be said for the CMTB Thwacker, which is bolted to a plate rather than pinned at the four corner holes. The presence of the base plate and bending rigidity of the bolts could increase the stiffness and natural frequencies of the Thwacker. Several holes in the Thwacker Frame and Tray were neglected, and the three components were bonded together instead of being preloaded with bolts. Both of these model simplifications could contribute to results that are stiffer than reality. As in the case of the Flight Thwacker, additional complexity would be required to improve the predictions of the response.

Effect of Operating Conditions On Performance

The Flight and CMTB Thwackers are both vibrated using a rotating eccentric mass. When the vibration is activated, the frequency and magnitude of the input force will increase from zero to the steady state operating level. The operating frequency for the Flight hardware is around 80 Hz, while both the QMDT and CMTB hardware operate at around 65 Hz. Both of these operating conditions are above the structural modes of the Flight Thwacker, and below the structural modes of the CMTB Thwacker. As the vibration frequency is increased from rest, the Flight Thwacker will pass through several natural frequencies. At the steady state operating conditions, the response is dominated by the sieve, and the sieve is essentially the same for both designs. Therefore, this analysis predicts that the performance of the CMTB Thwacker will be very similar to the Flight Thwacker within the expected steady state operating regime.

It is important to note that the presence of powder on the sieve drastically changes its dynamic response. As shown in Figure 12, the presence of powder tends to decrease the frequency at which a natural mode occurs. While the assumption that the powder remains effectively bonded to the sieve is unrealistic, some amount will stay in contact, so long as the lateral acceleration of the sieve is less than that of gravity. The powder will change the response of the sieve, but would likely have little effect on the structural modes of the hardware. Equivalent amounts of powder would behave similarly in the CMTB, QMDT, and Flight designs.

Previous research has suggested that lateral acceleration is the most important factor affecting the performance of sieves. To pass through a sieve, a particles must slide relative to the plane of the sieve. [4] This suggests that a there may be different options to optimize the efficiency of the sieve. The Flight sieve may operate better near the frequencies of the 9^{th} and 10^{th} modes, where the most lateral motion of the Thwacker Frame is expected, if allowed to by the requirements of other hardware. At the same time, higher frequencies and their associated mode shapes provide a larger number of node points where the lateral motion of the sieve is reduced. The reduced motion would allow more material to stay in contact with the sieve, and thus enable it to pass through.

5.0 Summary and Future Work

This analysis predicts that within their expected operating regime, the CMTB, QMDT, and Flight Thwacker designs will have equivalent sieving performance. The quality of this prediction could be improved with higher fidelity models of the hardware. Also, improvements in the effective material properties analysis would allow for a better approximation of the dynamic response of the sieve. Ideally, this analysis would be verified by operating all three hardware configurations between 0 and 100 Hz, while monitoring the acceleration of the Sieve Frame and displacement of the sieve itself. Such a test would allow the actual natural frequencies to be determined.

References

[1] Anderson, Robert C. et. all, “Particle transport and distribution on the Mars Science Laboratory mission: Effects of triboelectric charging,” *Icarus*, Vol. 204, 2009, pp. 545-557.

[2] Donachie, Matthew J. Jr., *Titanium A Technical Guide.* 2nd ed., ASM International, Materials Park, Ohio:, 2000, Chaps. 1.

[3] Federal Aviation Administration. *Metallic Materials Properties Development and Standardization, 5th Edition.* Handbook, Battelle Memorial Institute, 2010.

[4] Feller, R. and A. Foux. "Oscillating screen motion effect on the particle passage," *Transactions of the ASABE,* Vol. 18, No. 5, 1975, pp. 926-931.

[5] Li, Shuguang. "Boundary conditions for unit cells from periodic microstructures and their implications," *Composites Science and Technology,* Vol. 68, 2008, pp. 1962-1974.

[6] Lord Rayleigh, *Theory of Sound.* 2nd American ed., Dover Publications, New York, 1945.

[7] *Mars Science Laboratory Launch.* Press Kit, National Aeronautics and Space Administration (NASA), 2011.

[8] Timoshenko, S., *Vibration Problems in Engineering.* 3rd ed., D. Van Nostrand Company, Inc., Princeton, New Jersey, 1955.

[9] Young, Dana, "Vibration of Rectangular Plates by the Ritz Method," *Journal of Applied Mechanics,* Vol 17, 1950, pp. 448-453.